

# Effect of Long Waves on Ku-Band Ocean Radar Backscatter at Low Incidence Angles Using TRMM and Altimeter Data

Ngan Tran, B. Chapron, and D. Vandemark

**Abstract**—This letter uses a large ocean satellite data set to document relationships between Ku-band radar backscatter ( $\sigma_0$ ) of the sea surface, near-surface wind speed ( $U$ ), and ocean wave height (SWH). The observations come from satellite crossovers of the Tropical Rainfall Mapping Mission (TRMM) precipitation radar (PR) and two satellite altimeters, namely: 1) Jason-1 and 2) Environmental Satellite. At these nodes, we obtain TRMM clear-air normalized radar cross-section data along with coincident altimeter-derived significant wave height. Wind speed estimates come from the European Centre for Medium-Range Weather Forecast. TRMM PR is the first satellite to measure low incidence Ku-band ocean backscatter at a continuum of incidence angles from  $0^\circ$  to  $18^\circ$ . This letter utilizes these global ocean data to assess hypotheses developed in past theoretical and field studies—namely that variations in ocean sea state are measurably and systematically related to Ku-band  $\sigma_0$ , that the impact changes with incidence angle, and that it will affect the retrieval of wind speed from  $\sigma_0$ . Results have bearing on near-nadir ocean radar missions such as Surface Waves Investigation and Monitoring from Satellite, Advanced Scatterometer, TRMM, and the wide-swath altimeter.

**Index Terms**—Author, please supply your own keywords or send a blank e-mail to keywords@ieee.org to receive a list of suggested keywords.

## I. INTRODUCTION

SATELLITE radars are used to infer the wind speed just above the sea surface through their measurement of backscattered signal power, which is a signal that changes with the amount and steepness of ocean waves. This normalized radar backscatter cross-section ( $\sigma_0$ ) term also depends on the frequency, polarization, and incidence angle ( $\theta$ ) of the incident radiation. Two now-standard satellite systems for ocean wind estimation are the altimeter and the scatterometer. The former views the sea from a downlooking ( $\theta = 0^\circ$ ) incidence angle, whereas the latter uses side-looking angles from  $20^\circ$  to  $60^\circ$ . It is widely held that centimeter-scale ocean gravity-capillary waves and their growth or decay with wind forcing are the dominant controls of  $\sigma_0$  variation for both sensors, but the ocean reflection is distinctly different for these two systems that is consistent with the optical expectation; increased wave roughness

decreases altimeter  $\sigma_0$  but increases it for the scatterometer. This is because the incidence angle leads to differing scattering processes: dominant quasi-specular scattering for the former and Bragg resonance diffraction for the latter. Regardless of such differences, the linkage between  $\sigma_0$  and wind forcing is used for both sensors to empirically derive wind speed inversion algorithms that are well validated and widely used. However, long-wavelength tilting of short-scale waves is a known effect inducing fundamental perturbations in the precise relationship between local wind forcing and local radar backscatter variations. What is central for this letter is the acknowledgement that long-wave tilting of these short-scale waves is an additional second-order but fundamental perturbation that can impinge on any assumed direct relation between local wind forcing and radar backscatter variation, particularly at near-nadir incidence angles. A substantial fraction of the longer tilting gravity wave field is due to swell and wind seas generated by distant or turning winds, which are uncoupled and misaligned with the local wind.

Previous investigations have used bulk wave statistical parameters such as significant wave height (SWH) to demonstrate long-wave variability impacts upon  $\sigma_0$  [15], [22], [23], [29] and more widely on retrieved winds [12], [13], [21], [27], [28]. Such observations have clearly shown long-wave effects on altimeter backscatter and have led to the development of an operational wind speed model for the satellite altimeter that utilizes both  $\sigma_0$  and SWH [7], [13], where fortuitously both measurements are made from the same platform. SWH is not retrievable using scatterometry.

While altimeter ocean backscatter has been successfully modeled with quasi-specular scattering theory, off-nadir radar backscatter represents a mixture of specular and tilted Bragg resonance diffraction processes as the incidence angle extends away from  $0^\circ$  out toward  $10^\circ$ – $15^\circ$ . The transition between the two scattering regimes depends upon the instrument wavelength and the wind speed and has been proposed to occur near an incidence angle of  $10^\circ$ . A notable observation is that close to this angle a lower sensitivity between  $\sigma_0$  and wind speed is found [14], [19], [25]. This particular feature has been exploited over the ocean to calibrate airborne and spaceborne precipitation or cloud radars—the objective being to minimize uncertainty due to surface wind variations.

The low, or near-nadir, incidence angle range of  $1^\circ \leq \theta \leq 8^\circ$ , is currently covered by the precipitation radar (PR) on the Tropical Rainfall Mapping Mission (TRMM) [17], [18]. Though designed specifically for the measurement of precipitation profiles in the atmosphere over both land and ocean, 91

Manuscript received January 5, 2007; revised March 9, 2007.

N. Tran is with the Space Oceanography Division, Collecte Localisation Satellites, 31520 Ramonville St-Agne, France (e-mail: tran@cls.fr).

B. Chapron is with the Centre de Brest, French Research Institute for Exploration of the Sea (IFREMER), 29280 Plouzané, France.

D. Vandemark is with the Ocean Process Analysis Laboratory, University of New Hampshire, Durham, NH 03824 USA.

Digital Object Identifier 10.1109/LGRS.2007.896329

92 the PR system also acquires sea surface  $\sigma_0$  under rain-free  
 93 conditions. Using wind speed estimates from the TRMM Mi-  
 94 crowave Imager (TMI), a fully empirical model function was  
 95 built to relate cross section to wind speed for incidence angles  
 96 from  $0^\circ$  to  $18^\circ$  [11]. This is the first and only satellite system  
 97 to provide such angle-resolved scattering near nadir, and the  
 98 objective here is to further examine these data to help bridge  
 99 what is known regarding the effects of waves on the altimeter  
 100 and scatterometer. In this letter, we take the advantage of a  
 101 large collocated database, which is compiled using PR and both  
 102 Jason-1 and Environmental Satellite (ENVISAT) altimeters,  
 103 to extend the description of PR  $\sigma_0$  in terms of wind speed,  
 104 significant wave height, and incidence angle through a tabulated  
 105 model function  $\sigma_0(\theta, U, SWH)$ . This provides a compact and  
 106 statistically accurate representation permitting the study of the  
 107 expected wave tilting impacts on the sea surface scattering at  
 108 these low incidence angles.

## 109 II. DATA SETS

### 110 A. TRMM PR Cross Section

111 The TRMM satellite was launched in November 1997 car-  
 112 rying five instruments including the PR. Since the focus of  
 113 TRMM is to measure rainfall in the tropics, a low inclination  
 114 non-sun-synchronous orbit was selected to confine the satellite  
 115 ground track between  $35^\circ\text{S}$  and  $35^\circ\text{N}$ . The PR is a Ku-band  
 116 pulsed radar operating at 13.8 GHz and horizontal polarization.  
 117  $\sigma_0$  measurements are collected through the atmospheric column  
 118 and from the surface. The PR antenna is an electronically  
 119 scanned phased array that scans a plane normal to the flight  
 120 direction (cross-track) through the nadir with measurements at  
 121 49 beam positions (e.g., the angle bins 1, 25, and 49 correspond  
 122 to the incidence angles  $+18^\circ$ ,  $0.1^\circ$ , and  $-18^\circ$ , respectively) over  
 123 a 215-km ground swath. The scan duration is equal to 0.6 s with  
 124 a surface pixel provided every 4.3 km both along and cross-  
 125 track [16], [17] for the original orbit height.

126 The TRMM orbit was raised from 350 to 403 km in Au-  
 127 gust 2001 to increase the duration of the mission. The spatial  
 128 resolution of the PR is thus degraded slightly, increasing to  
 129 5.0 km by 5.0 km. Our data analysis covers the one-year  
 130 period of 2003. The high quality of the PR surface ocean  $\sigma_0$   
 131 data for this period was confirmed in two recent studies [11],  
 132 [31]. The data product used herein is TRMM PR standard  
 133 product 2A21 (ver. 5) from the Goddard Distributed Active  
 134 Archive Center. These data include normalized radar cross-  
 135 section measurements, associated quality flags, and a rain/no-  
 136 rain flag for each incidence angle bin or pixel [18]. Data over  
 137 land, with any data quality issue, or with rain over the ocean  
 138 target are all excluded from the composite data set. Further data  
 139 processing and satellite-to-satellite crossover selection details  
 140 follow [31] except that for this letter the search was performed  
 141 over all incidence angles in the PR ground tracks. As shown  
 142 in the previous study, the density of crossovers increases with  
 143 latitude due to the combined altimeter-PR orbit characteristics.

### 144 B. Wind Speed and Significant Wave Height Data

145 We use surface wind speed estimates ( $U$ ) from the surface  
 146 model analysis provided by the European Centre for Medium-

Range Weather Forecast (ECMWF) as a common reference to 147  
 quantify PR  $\sigma_0$  wind dependence. SWH data for the study come 148  
 from the Jason-1 and ENVISAT altimeters. These satellites 149  
 also provide an estimate of wind speed using altimeter  $\sigma_0$  150  
 measurements, but ECMWF model winds are used for the 151  
 model functions developed here explicitly because we do not 152  
 wish to introduce the known sea state impacts that lie within 153  
 altimeter wind speed data into the present PR results. The 154  
 potential negative impact of using the model wind products is 155  
 that these data are extracted and interpolated from six hourly 156  
 $1^\circ$  grid data set and that model winds will always disagree 157  
 with *in situ* measurements to a certain degree. Thus, the model 158  
 functions to be developed will be slightly impacted, particularly 159  
 at lightest wind speed, by this interpolation but previous studies 160  
 (e.g., [13]) have shown that the systematic nature of wave 161  
 height impacts should still be quite apparent and similar when 162  
 using the ECMWF model winds and it is this impact that is 163  
 the main focus of this letter. While one could go another step 164  
 to gather TRMM/scatterometer/altimeter triplet crossovers to 165  
 replace ECMWF winds with those from scatterometry, this 166  
 step dramatically reduces the data set size without dramatically 167  
 increasing the quality of the result as the agreement between 168  
 the ECMWF and scatterometer product is high. 169

Time/space interpolated ECMWF wind speed and standard 170  
 altimeter SWH estimates are both available in the Geophysical 171  
 Data Records (GDR) for these two altimeters. The Jason-1 172  
 altimetric mission was launched in December 2001 and placed 173  
 in the same ground track as its predecessor TOPEX/Poseidon. 174  
 It carries the Poseidon-2 altimeter that was derived from the 175  
 experimental Poseidon-1 instrument aboard TOPEX/Poseidon. 176  
 The satellite flies a nonsun-synchronous orbit at an altitude 177  
 of 1336 km with an inclination of  $66^\circ$ . Detailed description 178  
 of the mission and the Poseidon-2 instrument are provided, 179  
 respectively, in [20] and [5]. The ENVISAT altimeter (called 180  
 Radar Altimeter 2) was launched on March 2002 and is derived 181  
 from the European Remote Sensing satellite (ERS)-1 and ERS- 182  
 2 altimeters [2]. The satellite orbit is sun-synchronous at an 183  
 altitude of 800 km with an inclination of  $98.55^\circ$  allowing 184  
 measurement closer to the poles than Jason-1. More details can 185  
 be found in the ENVISAT product handbook [3]. Parameters 186  
 from both Jason-1 and ENVISAT GDRs over the one-year 187  
 period of 2003 are used for this letter. Erroneous altimeter 188  
 estimates are discarded using conventional data quality flag- 189  
 ging [3], [24]. Further data filtering follows from the Cal/Val 190  
 quality assessment that is routinely performed at the Collecte 191  
 Localisation Satellites [8]. We use only rain-free data. Since 192  
 the Jason-1 rain flag, which is currently available at the time of 193  
 this analysis, uses a TOPEX-derived algorithm that was not yet 194  
 fine-tuned on Jason-1 measurements, a Jason-1 rain flag was 195  
 calculated using a more recent algorithm [30]. This algorithm 196  
 shows higher sensitivity to low intensity rainfall as shown using 197  
 TMI rain estimates [33]. 198

### 199 C. Crossover Selection

The criteria used for the collocation between PR and Jason-1 200  
 or ENVISAT crossovers are given as follows: time separation 201  
 within 1 h and spatial separation less than 100 km. The different 202  
 collocation sets PR/altimeter/ECMWF are limited in latitude 203  
 to the tropics within  $\pm 35^\circ$  of the equator due to the TRMM 204

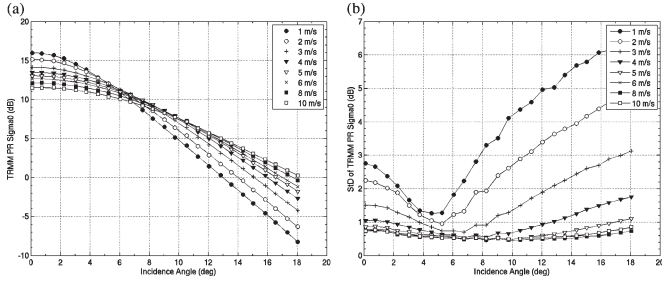


Fig. 1. (a) Mean values and (b) standard deviations of binned PR  $\sigma_0$  as a function of incidence angle for different wind speeds (SWH between 0.5 and 6.5 m).

205 orbit. We merge the two data sets using, respectively, Jason-1  
 206 and ENVISAT SWH estimates to obtain a unique data set  
 207 over which the geophysical model function  $\sigma_0(\theta, U, SWH)$  can  
 208 be produced. To insure homogeneity and consistency between  
 209 altimeter SWH estimates for the two missions, we applied small  
 210 [ $O$  (cm)] SWH adjustments per the most recent correction  
 211 model [26].

### 212 III. NEAR-NADIR SCATTERING MODEL

213 Following the standard quasi-specular backscattering ap-  
 214 proach, near-nadir  $\sigma_0$  can be written as

$$\sigma_0(\theta, U, SWH) = \frac{\rho(U)}{\text{mss}(U, SWH)} \sec^4(\theta) \exp\left[-\frac{\tan^2(\theta)}{\text{mss}(U, SWH)}\right] \quad (1)$$

215 where  $\sigma_0$  is the normalized backscatter in natural units (not in  
 216 decibels), and  $\theta$  is the incidence angle as previously defined.  
 217  $\rho$  represents an effective nadir reflection coefficient, and  $\text{mss}$   
 218 is a measure of the effective mean square slope (see [4] for  
 219 review). The model assumes that sea state dependence of  $\rho$  is  
 220 unlikely or negligible, which is verified to a large extent using  
 221 the dual frequency capabilities of the TOPEX altimeter [6], [9].  
 222 The model also allows for the impact of sea state on the cross  
 223 section. It is the overall degree of sea state development, which  
 224 contributes to the mean squared tilting slopes. Yet, the analogy  
 225 with optical scattering assumption implies that the incident  
 226 radiation wavelength should be much shorter than all roughness  
 227 lengths on the surface. For microwave probing of the ocean  
 228 surface, this is untrue due to the presence of gravity-capillary  
 229 waves. In particular, at first order and with a Gaussian statistical  
 230 assumption, the slope variance in (1) corresponds to a filtered  
 231 slope distribution [35].

232 As obtained in Fig. 1(a) (see also [11, Fig. 5]), the Gaussian  
 233 assumption of (1) is qualitatively consistent with the PR data  
 234 up to about  $18^\circ$ . Observed biases at nadir between altime-  
 235 ter measurements and PR data can be attributed to absolute  
 236 calibration issues [31]. According to (1), analysis of a single  
 237 frequency radar altimeter with both wind speed and sea state  
 238 proxy cannot, with certainty, separate the dependencies related  
 239 to  $\text{mss}$  variations from those related to variations of  $\rho$ . This is  
 240 because at nadir, (1) becomes

$$\sigma_0(\theta = 0, U, SWH) = \frac{\rho(U)}{\text{mss}(U, SWH)}. \quad (2)$$

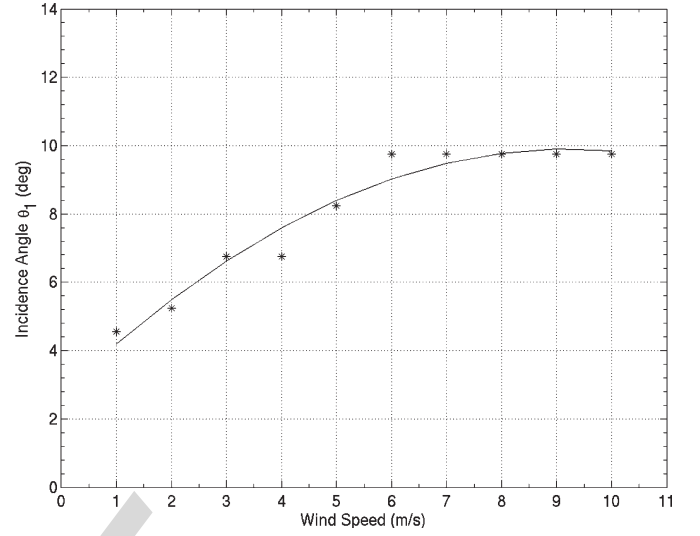


Fig. 2. Incidence angle  $\theta_1$  presenting the lowest standard deviation of binned PR  $\sigma_0$  at a given wind speed as function of wind speed. Overlaid is a quadratic regression fit to better display the trend.

Perhaps more interestingly, the differentiation of (1) with  
 respect to  $\text{mss}$  yields

$$\frac{\partial \sigma_0}{\partial \text{mss}} = \frac{\tan^2(\theta) - \text{mss}}{\text{mss}^2} \sigma_0. \quad (3)$$

The form of the fractional cross-section variation ( $\Delta\sigma_0/\sigma_0$ )  
 in natural units (not in decibels), due to fractional change of  
 $\text{mss}$ , will be incidence angle dependent, i.e., 1) when  $\tan^2(\theta) <$   
 $\text{mss}$ ,  $\Delta\sigma_0/\sigma_0 \propto (-\Delta\text{mss}/\text{mss})$  and the nadir viewing altimeter  
 falls in this category, and 2) at higher incidence angles, when  
 $\tan^2(\theta) > \text{mss}$ ,  $\Delta\sigma_0/\sigma_0 \propto (+\Delta\text{mss}/\text{mss})$  and the off-nadir  
 viewing scatterometer falls into this category. The following  
 analysis of the PR  $\sigma_0$  documents this fractional change of  $\sigma_0$   
 with incidence angle.

### IV. ANALYSIS OF PR BACKSCATTER

#### A. Geophysical Model Function for Ku-Band Ocean $\sigma_0$ at Low Incidence Angles

We restrict this letter to light-to-moderate wind speed condi-  
 tions up to 11 m/s. At wind speeds above this range, complex  
 nonlinear surface wave structure and foam involved with large-  
 scale wave breaking become critical to the surface description  
 and the radar scattering from it. While these higher winds are  
 important, the extensive amount of data that fall at or below  
 11 m/s and the physics associated with these conditions are the  
 focus of this letter. Two empirical tabular model functions are  
 developed. The first model is based on the analysis of measured  
 $\sigma_0$  at each PR incidence angle within specified wind speed  
 intervals and is denoted  $\sigma_0(\theta, U)$ . The 25 different incidence  
 angles are given as follows:  $0.1^\circ$  (nadir),  $0.75^\circ$ ,  $1.55^\circ$ ,  $2.25^\circ$ ,  
 $3.05^\circ$ ,  $3.75^\circ$ ,  $4.55^\circ$ ,  $5.25^\circ$ ,  $6.05^\circ$ ,  $6.75^\circ$ ,  $7.55^\circ$ ,  $8.25^\circ$ ,  
 $9.05^\circ$ ,  $9.75^\circ$ ,  $10.55^\circ$ ,  $11.30^\circ$ ,  $12.05^\circ$ ,  $12.85^\circ$ ,  $13.55^\circ$ ,  
 $14.35^\circ$ ,  $15.05^\circ$ ,  $15.85^\circ$ ,  $16.55^\circ$ ,  $17.35^\circ$ , and  $18.05^\circ$ , and the bin width is about  
 $0.1^\circ$ . The model is formed from the sample mean  $\sigma_0$  in each 1-  
 270 m/s wind speed and incidence angle 2-D bin. A  $3\sigma$  filter is then  
 applied to eliminate outlier measurements, giving Fig. 1(a). The  
 second model function takes into account both wind speed and

274 significant wave height dependence at each incidence angle. It  
275 is denoted as  $\sigma_0(\theta, U, SWH)$ . The wind speed bin width is still  
276 1 m/s, and the SWH bin width is set to 1 m.

### 277 B. $\sigma_0(\theta, U)$

278 Fig. 1(a) shows that results from nadir to  $5^\circ$  in incidence  
279 angle are monotonically decreasing in  $\sigma_0$  as wind speed in-  
280 creases. Above  $10^\circ$ ,  $\sigma_0$  becomes a monotonically increasing  
281 function of wind speed. In the range  $5^\circ \leq \theta \leq 10^\circ$ ,  $\sigma_0$  first  
282 increases, then decreases with increasing wind speed with a  
283 low sensitivity to wind speed. The standard deviations of the  
284  $\sigma_0$  measurements in each  $(\theta, U)$  bin are shown in Fig. 1(b)  
285 with respect to incidence angle for different wind speeds. For  
286 all wind speeds, standard deviations reach a minimum value  
287 at an incidence  $\theta_1$  between  $4^\circ$  and  $10^\circ$ . Higher magnitudes  
288 of standard deviation are associated with light wind speeds,  
289 and these magnitudes decrease with increasing wind speed.  
290 Magnitudes are smaller at nadir ( $0.1^\circ$ ) than at  $18^\circ$  for light  
291 wind speeds up to 5 m/s. Above 5 m/s, results show similar  
292 values. In the range  $4^\circ \leq \theta \leq 10^\circ$ ,  $\sigma_0$  not only exhibits low  
293 sensitivity to wind speed but also an overall low variability. This  
294 lowered variability is related to (3). The angle  $\theta_1$ , in Fig. 2,  
295 roughly identifies the condition  $\tan^2(\theta) = mss(U)$  for which  
296 the fractional cross-section variation is minimum, and the shift  
297 of  $\theta_1$  with wind speed corresponds to the anticipated increase of  
298 mss. As found, there is an increase of  $\theta_1$  with increasing wind  
299 speed up to 7 m/s followed by a saturation trend toward  $\sim 10^\circ$   
300 for higher moderate winds.

### 301 C. $\sigma_0(\theta, U, SWH)$

302 The very large collocated data set compiled enables the  
303 analysis of the combined incidence angle and SWH depen-  
304 dencies on  $\sigma_0$  using the narrow 1-m/s wind speed bin. Fig. 3  
305 displays a difference factor  $\delta$  defined as  $[\sigma_0(\theta, U, SWH) -$   
306  $\sigma_0(\theta, U)]$ , in decibels, with respect to incidence angle at four  
307 selected wind speeds of 2, 5, 7, and 10 m/s. For all winds,  
308 behavior of  $\delta$  as a function of SWH is clear. At low SWH  
309 ( $\sim 1$  m) representing young sea,  $\delta$  decreases with increasing  
310 angle, whereas for higher SWH ( $\sim 4$  m associated mostly with  
311 mixed seas including swell)  $\delta$  exhibits the opposite trend. The  
312 overall picture shows that at a given wind speed, all curves  
313 (linear least-squares fits) associated to the different 1-m SWH  
314 classes intersect at a particular value of incidence angle  $\theta_2$  that  
315 shifts with respect to wind speed value.

316 Very similar results are obtained when reducing the crossover  
317 collocation criteria. A subset is extracted for measurements  
318 collocated in time to within 1/2 h and 25 km in space. Fig. 4  
319 is the same as Fig. 3 but only for the case of two moderate  
320 wind speeds (7 and 10 m/s) for which there is still sufficient  
321 data (minimum of 100 samples per bin) to compute statistically  
322 stable indicators.

323 The relative magnitude of  $\sigma_0$  for extreme conditions, i.e., low  
324 and high SWH (1 and 4 m, respectively), is shown in Fig. 5 as a  
325 function of incidence angle for light-to-moderate wind speeds.  
326 For all wind speeds, we observe a positive magnitude at low  
327 incidence angles that decreases to reach a negative value at  
328 higher incidence. At 2-m/s wind, the magnitude is, respectively,  
329  $\sim 0.8$  dB at nadir and  $-1.6$  dB at  $\sim 18^\circ$ . At 10 m/s, we ob-  
330 serve almost similar absolute magnitude of variation ( $\sim 0.8$  dB)

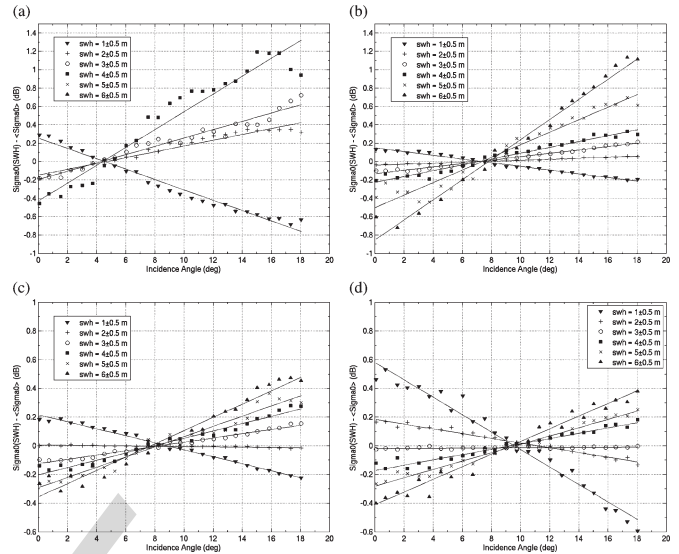


Fig. 3. Difference  $\delta$  (between averaged PR  $\sigma_0$  associated to a 1-m class of SWH and the averaged values estimated over all SWH) as function of incidence angles for various SWH classes at selected wind speeds: (a) 2 m/s, (b) 5 m/s, (c) 7 m/s, and (d) 10 m/s (1-m/s bin width). Overlaid are linear regression fits to better display the trends.

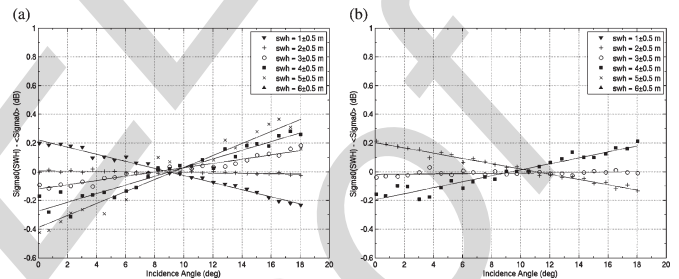


Fig. 4. Same as Fig. 3 but crossover data are selected with narrower selection criteria, 25 km and 30 min, for two selected wind speeds: (a) 7 m/s and (b) 10 m/s (1-m/s bin width).

between the two extreme incidence angles. These results are 331  
consistent with the previous analysis at higher incidence angles 332  
( $20^\circ$ ,  $30^\circ$ ,  $40^\circ$ , and  $60^\circ$ ) in [23] using NUSCAT-SWADE data. 333  
However, in cases of moderate winds, these authors concluded 334  
that the existence of large waves with high SWH will not have 335  
significant impact on the radar backscatter since the observed 336  
differences were within the uncertainty of the radar ( $\pm 1$  dB). 337  
The large amount of data available here helps to revise these 338  
conclusions. For these wind conditions, the presence of large 339  
waves significantly impact  $\sigma_0$  from nadir to  $18^\circ$  except around 340  
a particular incidence angle, denoted  $\theta_2$  in Fig. 6, where  $\sigma_0$  is 341  
insensitive to SWH at a given wind speed. As found,  $\theta_1$  and 342  
 $\theta_2$  angles are almost equal and correspond to the condition 343  
 $\tan^2(\theta_1) = \tan^2(\theta_2) = mss(U)$ . Around these critical angles, 344  
the backscatter cross section is insensitive to significant wave 345  
height variations at a given wind speed. 346

One point of note for these TRMM PR data is that they 347  
represent horizontally polarized returns. There is a recognized 348  
difference in the response of horizontal and vertical polarization 349  
returns from the sea surface (cf. [1]). The present results, in 350  
terms of overall features, can however be easily transposed to 351  
a vertically polarized result. Indeed, continuity between nadir 352  
viewing returns (no polarization) and scatterometer off-nadir 353  
returns in either one of the polarized states indicates that since 354

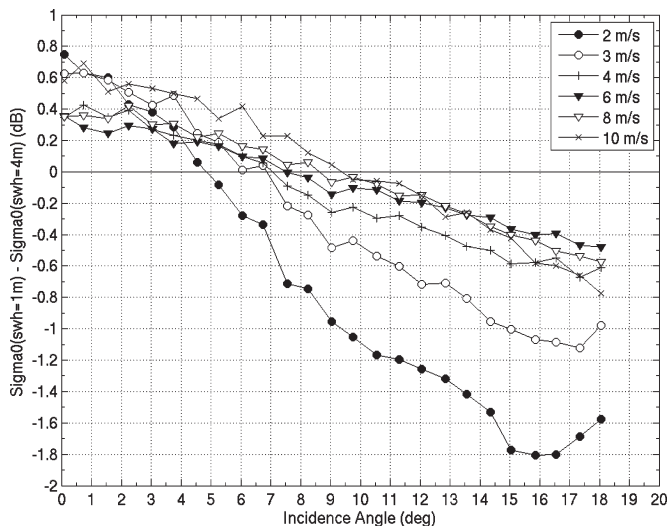


Fig. 5. Magnitude of the difference of  $\sigma_0$  between low SWH (1 m) and high SWH (4 m) conditions as function of incidence angle for different wind speeds from light to moderate winds.

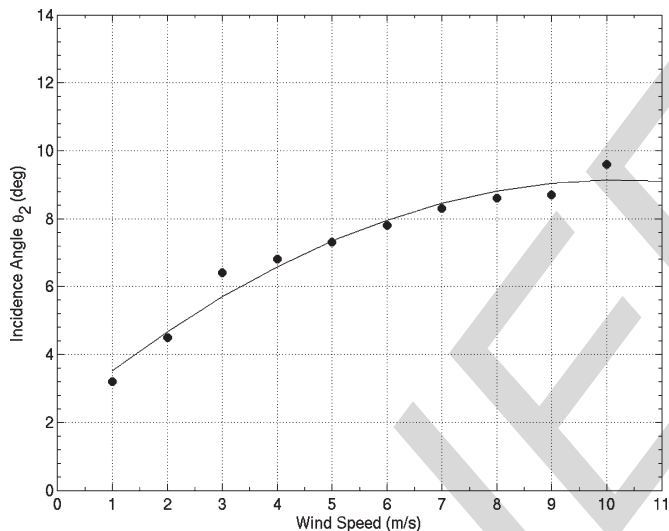


Fig. 6. Incidence angle  $\theta_2$  presenting a quasi-insensitivity of PR  $\sigma_0$  to SWH at a given wind speed as function of wind speed. Overlaid is a quadratic regression fit to better display the trend.

355 sea state effects are observed in both polarizations when the  
 356 backscatter is off nadir, all near-nadir measurements will dis-  
 357 play the same trends (in HH and VV). Previous analysis of the  
 358 National Aeronautics and Space Administration scatterometer  
 359 (NSCAT) backscatter in each polarization state shows similar  
 360 relative sea state impacts with respect to a global averaged  
 361 backscatter that was derived by mixing all sea state conditions;  
 362 they are slightly larger for NSCAT HH polarization measure-  
 363 ment than on VV polarization data regardless of incidence  
 364 angles between  $16^\circ$  and  $50^\circ$  [32].

365

V. CONCLUSION

366 New approaches for viewing the global ocean using satellites  
 367 have become available in the last decade. This letter focuses on  
 368 sea surface roughness remote sensing and what can be learned  
 369 using a multiple satellite perspective with the specific goal  
 370 being to provide new data to bridge the gap between what

is known about nadir and off-nadir microwave scattering and  
 371 emission from the ocean. Near-surface wind speed is a first-  
 372 order geophysical parameter to be derived from microwave  
 373 ocean sensors (the scatterometer, radiometer, and altimeter), but  
 374 it is well known that the transfer function between their raw  
 375 measurements and wind speed must account for perturbation  
 376 due to surface wave processes that often deviate from simple  
 377 local wind forcing behavior. To reduce uncertainties in satellite  
 378 wind speed retrieval from backscatter measured at different  
 379 observation angles and to ensure proper assimilation of scat-  
 380 terometer and altimeter data into numerical weather prediction  
 381 models, it is increasingly apparent that a precise understanding  
 382 of the relationship between surface roughness through radar  
 383 backscatter measurement and both wind and wave conditions  
 384 is very important [28], [29]. Gaining quantitative insight on  
 385 these sea state perturbations using field studies is notoriously  
 386 difficult due to the inability to gather the sufficient range of  
 387 surface conditions and data population.

388  
 This letter makes use of a multisatellite ocean observing  
 389 opportunity, where a new type of ocean surface remote sensing  
 390 data set, i.e., the TRMM cross-track scanning radar, is com-  
 391 bined with coincident sea surface wave height information from  
 392 crossing satellite altimeters to provide all-new data illustrat-  
 393 ing wave impacts on radar backscatter at multiple incidence  
 394 angles. The resulting TRMM PR model function provides  
 395 results showing that long-wave tilting effects are quantitatively  
 396 confirmed in line with recent airborne slope measurements [34].  
 397 Accordingly, near-nadir cross-section measurements at a given  
 398 fixed wind speed and ranging in incidence angles out to  $20^\circ$  are  
 399 measurably related to the sea state dynamics. As a surrogate for  
 400 the sea state's degree of development, the use of a collocated  
 401 SWH parameter helps to document this impact and to clearly  
 402 identify the off-nadir incidence angle that corresponds to the  
 403 lowest fractional cross-section variation—a very useful angle to  
 404 know in over-ocean radar calibration activities. For TRMM PR  
 405 incidence angles that lie closer to scatterometer viewing angles  
 406 (i.e.,  $16^\circ$ – $20^\circ$ ), our results show that for light-to-moderate  
 407 wind conditions the presence of large waves can affect the perfor-  
 408 mance of surface wind retrieval algorithms, which is consis-  
 409 tent with previous results (e.g., [27] and [29]). As expected,  
 410 larger incidence angles are thus certainly to be recommended  
 411 for surface wind scatterometry to minimize sea state impact.  
 412 Combined use of both nadir and near-nadir single frequency  
 413 measurements can also help to infer a sea surface slope variance  
 414 that can potentially be related to surface wind stress [35] and  
 415 assimilated into numerical wave models. As obtained, this sea  
 416 surface slope variance will include both longer wave and shorter  
 417 wave slope contributions. Dual frequency nadir measurements  
 418 and/or use of the contemporaneous SWH measurements will  
 419 then help to remove the longer wave contributions to leave the  
 420 shorter ones [9]. At nadir and near-nadir configurations, dual  
 421 frequency capability will thus improve short surface wave ob-  
 422 servations and surface wind retrieval algorithm performances.

424

ACKNOWLEDGMENT

The authors would like to thank the Goddard Space Flight  
 425 Center Distributed Active Archive Center for the straightfor-  
 426 ward and rapid electronic access to the TRMM PR data. The  
 427 authors would also like to thank two anonymous reviewers  
 428 whose comments helped improve the clarity of the document.

429

## REFERENCES

- 430
- 431 [1] C. Anderson, T. Macklin, C. Gommenginger, M. Srokosz, J. Wolf, and  
432 J. Hargreaves, "Impact of sea state on nadir-looking and side-looking  
433 microwave backscatter," *Earth Observation Quart.*, no. 67, pp. 5–8, 2000.
- 434 [2] J. Benveniste, M. Roca, P. Vincent, G. Levrini, S. Baker, O.-Z. Zanife, and  
435 C. Zelli, "The Envisat radar altimetry mission: RA-2, MWR, DORIS and  
436 LRR," *ESA Bull.*, vol. 105, pp. 67–76, 2001.
- 437 [3] J. Benveniste, S. Baker, O. Bombaci, C. Zeli, P. Venditti, O.-Z. Zanife,  
438 B. Soussi, J.-P. Dumont, J. Stum, and M. Pilar Milagro-Perez, *Envisat  
439 RA-2/MWR Product Handbook*. Frascati, Italy: Eur. Space Agency,  
440 2002. PO-TN-ESR-RA-0050. [Online]. Available: [http://envisat.esa.  
441 int/dataproducts/ra2-mwr/CNTR.htm](http://envisat.esa.int/dataproducts/ra2-mwr/CNTR.htm).
- 442 [4] G. S. Brown, "Quasi-specular scattering from the air-sea interface," in  
443 *Surface Waves and Fluxes*, vol. 2, W. Plant and G. Geerneck, Eds. Nor-  
444 well, MA: Kluwer, 1990, pp. 1–40.
- 445 [5] G. Carayon, N. Steunou, J.-L. Courriere, and P. Thibaut, "Poseidon-2  
446 radar altimeter design and results of in-flight performances," *Mar. Geod.*,  
447 vol. 26, no. 3/4, pp. 159–165, Dec. 2003.
- 448 [6] B. Chapron, K. Katsaros, T. Elfouhaily, and D. Vandemark, "A note on  
449 relationships between sea surface roughness and altimeter backscatter,"  
450 in *Air-Water Gas Transfer*, B. Jähne and E. C. Monahan, Eds. Hanau,  
451 Germany: AEON Verlag & Studio, 1995, pp. 869–878.
- 452 [7] F. Collard and S. Labroue, "New wind speed algorithm for Jason-1,"  
453 presented at the Ocean Surface Topography Science Team Meeting,  
454 St. Petersburg, FL, Nov. 2004.
- 455 [8] J. Dorandeu, M. Ablain, Y. Faugère, F. Mertz, B. Soussi, and  
456 P. Vincent, "Jason-1 global statistical evaluation and performance  
457 assessment—Calibration and cross-calibration results," *Mar. Geod.*,  
458 vol. 27, no. 3/4, pp. 345–372, 2004.
- 459 [9] T. Elfouhaily, D. Vandemark, J. Gourrion, and B. Chapron, "Estimation  
460 of wind stress using dual-frequency TOPEX data," *J. Geophys. Res.*,  
461 vol. 103, no. C11, pp. 25 101–25 108, 1998.
- 462 [10] J. Figa-Saldana, J. J. W. Wilson, E. Attema, R. Gelsthorpe,  
463 M. R. Drinkwater, and A. Stoffelen, "The advanced scatterometer  
464 (ASCAT) on the meteorological operational (MetOp) platform: A follow  
465 on for European wind scatterometers," *Can. J. Remote Sens.*, vol. 28,  
466 no. 3, pp. 404–412, 2002.
- 467 [11] M. H. Freilich and B. A. Vanhoff, "The relationship between winds,  
468 surface roughness, and radar backscatter at low incidence angles from  
469 TRMM precipitation radar measurements," *J. Atmos. Ocean. Technol.*,  
470 vol. 20, no. 4, pp. 549–562, Apr. 2003.
- 471 [12] R. Glazman and A. Greysukh, "Satellite altimeter measurements of sur-  
472 face wind," *J. Geophys. Res.*, vol. 98, no. C2, pp. 2475–2484, Feb. 1993.
- 473 [13] J. Gourrion, D. Vandemark, S. Bailey, B. Chapron, C. P. Gommenginger,  
474 P. G. Challenor, and M. A. Srokosz, "A two-parameter wind speed  
475 algorithm for Ku-band altimeters," *J. Atmos. Ocean. Technol.*, vol. 19,  
476 no. 12, pp. 2030–2048, Dec. 2002a.
- 477 [14] V. Hesany, W. J. Plant, and W. C. Keller, "The normalized radar cross  
478 section of the sea at 10° incidence," *IEEE Trans. Geosci. Remote Sens.*,  
479 vol. 38, no. 1, pp. 64–72, Jan. 2000.
- 480 [15] W. C. Keller and W. J. Plant, "Cross-sections and modulation transfer  
481 functions at L and Ku-bands measured during the tower ocean wave  
482 and radar dependence experiment," *J. Geophys. Res.*, vol. 95, no. C9,  
483 pp. 16 277–16 289, 1990.
- 484 [16] T. Kozu *et al.*, "Development of precipitation radar onboard the tropi-  
485 cal rainfall measuring mission (TRMM) satellite," *IEEE Trans. Geosci.  
486 Remote Sens.*, vol. 39, no. 1, pp. 102–116, Jan. 2001.
- 487 [17] C. Kummerow, W. Barnes, T. Kozu, J. Shiue, and J. Simpson, "The  
488 tropical rainfall measuring mission (TRMM) sensor package," *J. Atmos.  
489 Ocean. Technol.*, vol. 15, no. 3, pp. 809–817, Jun. 1998.
- [18] C. Kummerow *et al.*, "The status of the tropical rainfall measuring mission  
490 (TRMM) after two years in orbit," *J. Appl. Meteorol.*, vol. 39, no. 12, 491  
pp. 1965–1982, Dec. 2000. 492
- [19] H. Masuko, K. Okamoto, M. Shimada, and S. Niwa, "Measurement of  
493 microwave backscattering signatures of the ocean surfaces using X and  
494 Ka-band airborne scatterometers," *J. Geophys. Res.*, vol. 91, no. C11, 495  
pp. 13 065–13 083, 1986. 496
- [20] Y. Menard, L.-L. Fu, P. Escudier, F. Parisot, J. Perbos, P. Vincent,  
497 S. Desai, B. Haines, and G. Kunstmann, "The Jason-1 mission," *Mar.  
498 Geod.*, vol. 26, no. 3/4, pp. 131–146, 2003. 499
- [21] F. Monaldo and E. Dobson, "On using significant wave height and radar  
500 cross section to improve radar altimeter measurements of wind speed,"  
501 *J. Geophys. Res.*, vol. 94, no. C9, pp. 12 699–12 701, Sep. 1989. 502
- [22] S. V. Nghiem, F. K. Li, and G. Neumann, "The dependence of ocean  
503 backscatter at Ku-band on oceanic and atmospheric parameters," *IEEE  
504 Trans. Geosci. Remote Sens.*, vol. 35, no. 3, pp. 581–600, May 1997. 505
- [23] S. V. Nghiem, F. K. Li, S. H. Lou, G. Neumann, R. E. McIntosh,  
506 S. C. Carson, J. R. Carswell, E. J. Walsh, M. A. Donelan, and  
507 W. M. Drennan, "Observations of ocean radar backscatter at Ku and  
508 C-bands in the presence of large waves during the surface wave dynamics  
509 experiment," *IEEE Trans. Geosci. Remote Sens.*, vol. 33, no. 3, pp. 708–  
510 721, May 1995. 511
- [24] N. Picot, K. Case, S. Desai, and P. Vincent, *AVISO and PODAAC User  
512 Handbook IGDR and GDR Jason Products*, 2003. SMM-MU-M5-OP-  
513 13184-CN (AVISO), JPL D-21352 (PODAAC). [Online]. Available:  
514 [www-aviso.cis.fr/documents/  
515 donnees/produits/handbook\\_jason.pdf](http://www-aviso.cis.fr/documents/donnees/produits/handbook_jason.pdf).
- [25] W. J. Plant, "Studies of backscattered sea return with a CW, dual-  
516 frequency, X-band radar," *IEEE Trans. Antennas Propag.*, vol. AP-25,  
517 no. 1, pp. 28–36, Jan. 1977. 518
- [26] P. Queffeuilou, "Long-term validation of wave height measurements from  
519 altimeters," *Mar. Geod.*, vol. 27, no. 3/4, pp. 495–510, 2004. 520
- [27] P. Queffeuilou, B. Chapron, and A. Bentamy, "Comparing Ku-band  
521 NSCAT scatterometer and ERS-2 altimeter winds," *IEEE Trans. Geosci.  
522 Remote Sens.*, vol. 37, no. 3, pp. 1662–1670, May 1999. 523
- [28] Y. Quilfen, B. Chapron, and D. Vandemark, "On the ERS scatterometer  
524 wind measurements accuracy: Evidence of seasonal and regional biases,"  
525 *J. Atmos. Ocean. Technol.*, vol. 18, pp. 1684–1697, 2001. 526
- [29] Y. Quilfen, B. Chapron, F. Collard, and D. Vandemark, "Relationship  
527 between ERS scatterometer measurement and integrated wind and wave  
528 parameters," *J. Atmos. Ocean. Technol.*, vol. 21, no. 2, pp. 368–373,  
529 Feb. 2004. 530
- [30] J. Tournadre, "Validation of Jason and Envisat altimeter dual-frequency  
531 rain flags," *Mar. Geod.*, vol. 27, no. 1/2, pp. 153–169, 2004. 532
- [31] N. Tran, O.-Z. Zanife, B. Chapron, D. Vandemark, and P. Vincent, "Ab-  
533 solute calibration of Jason-1 and Envisat altimeter Ku-band radar cross  
534 section from cross-comparison with TRMM precipitation radar measure-  
535 ments," *J. Atmos. Ocean. Technol.*, vol. 22, no. 9, pp. 1389–1402, 2005a. 536
- [32] N. Tran, "Contribution to analysis of NSCAT and ERS-2 scatterometer  
537 data by using neural network methodology—Sea state impact on scat-  
538 terometer returns," Ph.D. dissertation, Univ. Pierre et Marie Curie, Paris,  
539 France, 1999. 540
- [33] N. Tran, E. Obligis, and F. Ferreira, "Comparison of two Jason-1 altimeter  
541 precipitation detection algorithms with rain estimates from TRMM mi-  
542 crowave imager," *J. Atmos. Ocean. Technol.*, vol. 22, no. 6, pp. 782–794,  
543 2005b. 544
- [34] D. Vandemark, B. Chapron, J. Sun, G. H. Crescenti, and H. B. Graber,  
545 "Ocean wave slope observations using radar backscatter and laser altime-  
546 ters," *J. Phys. Oceanogr.*, vol. 34, no. 12, pp. 2825–2842, 2004. 547
- [35] D. Vandemark, J. B. Edson, and B. Chapron, "Altimeter estimation of  
548 sea surface wind stress for light to moderate winds," *J. Atmos. Ocean.  
549 Technol.*, vol. 14, no. 3, pp. 716–722, Jun. 1997. 550

## AUTHOR QUERIES

AUTHOR PLEASE ANSWER ALL QUERIES

AQ1 = Please provide keywords.

AQ2 = Please provide the expanded form of “NUSCAT-SWADE”.

AQ3 = Please check if the changes made to this sentence are correct. If not, kindly make the necessary adjustments.

Notes: 1) “ESA publications” was deleted in Ref. [2]. Please check.

2) Ref. [10] was uncited anywhere in the text. Please insert where appropriate.

ATTN: If you are paying to have all or some of your figures appear in color in the print issue, it is very important that you fill out and submit a copy of the IEEE Page Charge & Reprint Form along with your proof corrections. This form is available from the same URL where these page proofs were downloaded from. Thank you

END OF ALL QUERIES

IEEE  
Proof